



Cite this: *Soft Matter*, 2026, 22, 1551

## Order–disorder transition in soft and deformable particle assembly with dynamic size-dispersity in two dimensions

Rahul Kumar,  Sangwoo Lee  and Patrick T. Underhill \*

Soft and deformable objects are widespread in natural and synthetic systems, including micellar domains, microgel particles, foams, and biological cells. Understanding their phase behavior at high concentrations is crucial for controlling long-range order. Here, we employ a Voronoi-based model to study the packing of deformable particles in two dimensions under thermal fluctuations. Particles are represented as interconnected polygons, with the system energy comprising penalties for deviations in area and perimeter from preferred values. The strengths of these penalties capture two key features of packing: dynamic size dispersity, mimicking chain exchange in block copolymer micelles or solvent exchange in microgels, and particle line tension, reflecting the energy cost of shape changes. The model exhibits an order–disorder transition (ODT): low perimeter penalties yield disordered states, while higher penalties produce a hexagonal crystal lattice. Large dynamic size dispersity shifts the ODT to higher perimeter penalties. We explain this by analyzing particle sizes, defect formation barriers, and Voronoi entropy, which show that defect formation is easier when the area penalty term is smaller, providing a mechanistic basis for the ODT trends. In regimes far from ODT, deviations from the hexagonal lattice are accurately described by normal mode displacement fields, confirming that thermal fluctuations rather than defects govern the structure.

Received 31st October 2025,  
Accepted 11th January 2026

DOI: 10.1039/d5sm01097g

[rsc.li/soft-matter-journal](http://rsc.li/soft-matter-journal)

## 1 Introduction

Materials composed of soft and deformable constituent particles are ubiquitous in both natural and synthetic systems. Examples of such deformable particles include grafted core-shell particles,<sup>1–4</sup> dendrimers,<sup>5,6</sup> star polymers,<sup>7,8</sup> block copolymer micelles,<sup>9–11</sup> vesicles,<sup>12,13</sup> microgels,<sup>14,15</sup> emulsions,<sup>16,17</sup> foams,<sup>18</sup> and biological cells.<sup>19,20</sup> A key characteristic of deformable particles is their ability to shrink and/or deform in response to interactions with neighboring particles under crowded conditions. For example, densely packed microgels exhibit faceting and interpenetration of polymer chains,<sup>15,21</sup> and can nearly eliminate interstitial voids, thereby approaching space-filling configurations. Collectively, these physical systems can be modeled as a packing of soft, deformable particles. By contrast, particles such as silica microspheres and metallic nanoparticles are significantly less deformable. The maximum packing efficiency of monodisperse hard spheres is limited to ~74% in three dimensions, forming close-packed structures such as a face-centered cubic structure, and to ~91% for hard discs in a hexagonal close-packed arrangement in two dimensions. The packing of hard particles has been the subject of

extensive theoretical, computational, and experimental investigation over several decades.<sup>22–24</sup> In comparison, the packing behavior of deformable particles remains far less understood, despite its relevance to diverse soft-matter and biological systems.<sup>15,16,21</sup>

Owing to their deformability, such particles can adapt their shape in response to external stimuli, enabling the design of adaptive materials for stretchable electronics, soft robotics, and responsive surfaces.<sup>25</sup> Thin film self-assembly studies have direct applications in advanced coatings and membranes to functional interfaces.<sup>26</sup> Moreover, quasi-2D studies, particularly through simulations and model experiments, have provided fundamental insights into jamming, collective dynamics, and melting in two dimensions,<sup>27–29</sup> which often differ from their three-dimensional counterparts. Two-dimensional melting, in particular, has attracted considerable recent attention, especially with respect to the possible existence of intermediate hexatic phases and the nature of the melting transition, including continuous *versus* weak first-order scenarios.<sup>28,30</sup> Recent efforts have also focused on understanding the packing behavior of hard disks with static polydispersity.<sup>31,32</sup> In contrast, the impact of dynamic size dispersity on the packing structure remains relatively underexplored, despite its widespread relevance in experimental systems where particle sizes can fluctuate. For instance, the size of block copolymer micelles can

Department of Chemical and Biological Engineering, Rensselaer Polytechnic Institute, Troy, New York 12180, USA. E-mail: [underp3@rpi.edu](mailto:underp3@rpi.edu)



fluctuate due to the exchange of copolymer chains between micelles,<sup>33</sup> and microgel particles can swell or de-swell in a solvent, thereby altering their size within dense packings.<sup>34</sup>

To understand packing behavior, it is instructive to distinguish between packing and tiling, a distinction that becomes essential in nearly confluent assemblies of deformable particles. Packing refers to the arrangement of objects within a space, whereas tiling describes the partitioning of that space into distinct, non-overlapping compartments. In nearly confluent systems of densely packed deformable particles, the distinction between packing and tiling vanishes, as particle deformation allows them to collectively fill space without significant voids. In this regime, many-body interactions naturally emerge,<sup>1,35</sup> breaking down the common simplifying assumption of pairwise additivity that is often employed in computational simulations. To capture these collective effects, several modeling frameworks have been developed, including machine learning approaches for polymer-grafted nanoparticles,<sup>1,2,35</sup> deformable particle models representing particles as 2D spring rings,<sup>36</sup> and Vertex<sup>19,37–39</sup> and Voronoi-based<sup>40,41</sup> models commonly used to describe epithelial monolayers with polygonal cells.

In this study, we adopt a Voronoi-based model to investigate the packing behavior of soft and deformable particles in 2D where Voronoi cells represent the faceted polygonal particles under dense packing. We sample the system configurations from Boltzmann distributions at a fixed temperature, quantifying the effect of thermal fluctuations on the self-assembly. We further examine the impact of dynamic size dispersity on phase behavior, mimicking experimental scenarios in which the size of constituent particles fluctuates. We quantify topological defects in such systems and show their effect on the order of the system. Finally, we perform normal mode analysis of the ordered structures and discuss the resemblance between our model and the harmonic spring network.

## 2 Materials and methods

### 2.1 Voronoi model

We adopt a Voronoi-based model to simulate the 2D assembly of densely packed (no gaps between particles) soft and deformable particles. The phase behavior of such dense packings has been explored previously in three dimensions.<sup>42,43</sup> In the model, the Voronoi diagram represents the system configuration with Voronoi cells describing the faceted deformed particles. The Voronoi and Vertex models are closely related. While polygon centers serve as the degrees of freedom in the Voronoi model, polygon vertices are the degrees of freedom in the Vertex model. The energy of the system in our Voronoi model is given by the following expression:

$$E = \sum_{i=1}^N \left[ \frac{1}{2} k (A_i - A_0)^2 + \gamma (P_i - P_{ci}) \right] \quad (1)$$

where  $N$  is the total number of particles. The first term in the energy equation captures the area elasticity and imposes an

energy penalty when the instantaneous area  $A_i$  of the particle  $i$  deviates from its preferred area  $A_0$  and  $k$  controls the strength of the penalty, thereby controlling the degree of dynamic area-dispersity (size-dispersity) of the assembly in the system. The second term quantifies the perimeter penalty on the particle whose instantaneous perimeter  $P_i$  deviates from the preferred perimeter  $P_{ci}$  which is taken as the perimeter of an equivalent circle of area  $A_i$ , *i.e.*,  $P_{ci} \equiv 2\sqrt{\pi A_i}$ . The strength of the perimeter penalty is controlled by the line tension,  $\gamma$ . The choice of  $P_{ci}$  reflects that an isotropic circle geometry has the minimum perimeter density for the lowest line tension energy. The parameters  $k$  and  $\gamma$  capture two key aspects of packing behavior in soft, deformable particles. In experiments,  $k$  scales the energy penalty by the particle size fluctuations—accounting for chain exchange in block copolymer micelles and the resulting size dispersity—while  $\gamma$  quantifies particle deformability *via* the energy cost of shape changes. For example, in emulsion systems,  $\gamma$  can be mapped onto the effective interfacial tension of emulsion droplets, while in polymeric microgels or block copolymer micelles,  $\gamma$  reflects the energetic cost of particle deformation arising from polymer stretching.

We nondimensionalize the quantities in eqn (1) by scaling energies with thermal energy  $k_B T$ , where  $k_B$  is Boltzmann's constant and  $T$  is absolute temperature, and by scaling lengths with  $A_0^{1/2}$ . In nondimensional form, eqn (1) becomes

$$\tilde{E} = \sum_{i=1}^N \left[ \frac{1}{2} \tilde{k} (\tilde{A}_i - 1)^2 + \tilde{\gamma} (\tilde{P}_i - \tilde{P}_{ci}) \right] \quad (2)$$

where  $\tilde{E} = E/k_B T$ ,  $\tilde{k} = k A_0^2 / k_B T$ ,  $\tilde{A}_i = A_i / A_0$ ,  $\tilde{\gamma} = \gamma A_0^{1/2} / k_B T$ ,  $\tilde{P}_i = P_i / A_0^{1/2}$ , and  $\tilde{P}_{ci} = P_{ci} / A_0^{1/2}$ . Quantities denoted with tildes are dimensionless, and this convention is used consistently throughout the paper.

### 2.2 Monte Carlo simulations

We performed Monte Carlo (MC) simulations in the canonical ensemble for a two-dimensional system of  $N = 3600$  particles. The simulation box dimensions were set to  $55.836 \times 64.476$ , ensuring a preferred area of one in dimensionless units per particle. Also, the box dimensions are commensurate with a hexagonal crystal lattice. Periodic boundary conditions were applied along both the  $x$ - and  $y$ -directions. Each Monte Carlo move consisted of selecting a particle at random and displacing it by a random vector with magnitude up to a prescribed maximum displacement. After every move, we constructed the Voronoi tessellation of the particle configuration, using particle positions as the centers. This was implemented with MATLAB's "delaunayTriangulation" library.<sup>44</sup> The system energy was evaluated from the Voronoi diagram using eqn (2), and equilibrium configurations were sampled *via* the standard Metropolis algorithm. We refer to these as "thermal systems," reflecting the inclusion of thermal energy in the simulations. Based on eqn (2), increasing  $\tilde{k}$  or  $\tilde{\gamma}$  reduces the relative thermal energy in the system and *vice versa*. The maximum displacement was chosen such that the acceptance ratio lies in the range of 30–60%. We equilibrated our system for at least 40 000 Monte



Carlo cycles where one cycle consists of  $N$  displacement moves. At least 100 simulation snapshots, evenly sampled from 20 000 Monte Carlo cycles in the production run, were used to calculate the ensemble average of thermodynamic properties. Errors were estimated as the standard deviation of five block averages from the mean.

We investigate the phase behavior of particles interacting with the energy functional expressed in eqn (2) in three different regimes of dynamic size-dispersity. To do so, we choose three different values of  $\tilde{k}$  to obtain different degrees of dynamic size-dispersity in the system,  $\tilde{k} = 1000$ ,  $\tilde{k} = 100$ ,  $\tilde{k} = 30$ , to ensure low, moderate, and high dynamic size-dispersity, respectively. The initial configurations for Monte Carlo simulations were prepared in a perfect hexagonal lattice, oriented such that the two farthest-separated vertices of any hexagon lie along the  $x$ -axis. Three series of simulation runs were carried out with  $\tilde{k} = 1000$ ,  $\tilde{k} = 100$ ,  $\tilde{k} = 30$ , each over a range of  $\tilde{\gamma}$  values. Since energy is scaled by the thermal energy, a decrease in  $\tilde{\gamma}$  corresponds to an increase in the relative thermal energy of the system. To examine the system-size effect, we also simulated systems with  $N = 900$  and  $N = 2500$  in the boxes with dimensions commensurate with a hexagonal crystal lattice for the case of  $\tilde{k} = 100$  at varying values of  $\tilde{\gamma}$  (see Fig. S1 in the SI). The system behavior appears to be independent of system size. We chose a moderate system size of  $N = 3600$  to focus on the two dominant phases of interest, ordered and disordered, that are robustly captured within this regime. We also assessed the influence of initial conditions on the equilibrium phases (see Fig. S2 in the SI). Simulations initialized from both a perfect hexagonal lattice and a configuration obtained after equilibrating at nearby values of  $\tilde{\gamma}$  converge to the same equilibrium state, demonstrating robustness to initial conditions enabled by sufficient Monte Carlo sampling.

### 2.3 Structure factor

We characterize the system structure by computing the structure factor  $S(\vec{q})$  of the particle assembly by

$$S(\vec{q}) = \frac{1}{N} \left\langle \left| \sum_{i=1}^N e^{i\vec{q}\cdot\vec{r}_i} \right|^2 \right\rangle \quad (3)$$

where  $\vec{r}_i$  is the position vector of the Voronoi center of the  $i$ th particle,  $N$  is the total number of particles in the system,  $\vec{q}$  is a wave vector, and  $\langle \dots \rangle$  denotes an average over at least 100 evenly spaced simulation snapshots. The allowed wave vectors were determined by discretizing the simulation box spatially into  $300 \times 300$  grids. Then, we obtain azimuthally averaged  $S(\tilde{q})$  from  $S(\vec{q})$  where  $\tilde{q}$  is the magnitude of  $\vec{q}$ . For this,  $\tilde{q}$  was assigned to discrete radial bins spanning the desired  $\tilde{q}$ -range. Within each bin, the corresponding  $S(\vec{q})$  values were averaged to yield the powder-averaged  $S(\tilde{q})$ .

### 2.4 Orientational order parameter

We characterized the system structure by quantifying the hexatic order in the system since the honeycomb structure of

uniform hexagons has the least line tension energy.<sup>45</sup> We compute the local bond-orientational order parameter  $\psi_6$  for each particle using eqn (4).

$$\psi_{6,i} = \frac{1}{z_i} \sum_{j=1}^{z_i} e^{i6\theta_{ij}} \quad (4)$$

$$\Psi_6 = \left\langle \frac{1}{N} \sum_{i=1}^N \psi_{6,i} \right\rangle \quad (5)$$

In the eqn,  $i$  is the particle identity,  $z_i$  is the coordination number of the  $i$ th particle (same as the number of vertices of the particle),  $\theta_{ij}$  is the angle between the positive  $x$ -axis and the vector joining the Voronoi center of the particle to the vertex  $j$ . We refer to  $\theta_{ij}$  as the vertex angle. In the expression, 6 denotes the six-fold (hexatic) symmetry of the regular hexagon. By construction,  $\psi_{6,i}$  is a complex number, where the magnitude  $|\psi_{6,i}|$  quantifies the local six-fold order of the particle, and the phase  $\arg(\psi_{6,i})$  indicates the orientation of the particle relative to the positive  $x$ -axis. After computing  $\psi_6$  for all the particles, we obtain the mean global bond orientational order parameter  $\Psi_6$  of a system configuration by using eqn (5) where  $\langle \dots \rangle$  denotes an average over at least 100 evenly spaced simulation snapshots. For our initial configuration where two farthest-separated vertices of hexagons lie along the  $x$ -axis,  $\text{Im}(\Psi_6)$ , the imaginary component of  $\Psi_6$ , is zero, and  $\text{Re}(\Psi_6)$ , the real component of  $\Psi_6$ , is one. Moreover, for a completely disordered arrangement of polygons under the constraint where the mean coordination number of polygons is 6,  $\Psi_6$  is essentially zero.

### 2.5 Voronoi entropy

We also compute the Voronoi entropy  $S_{\text{vor}}$  which is the Shannon entropy of the Voronoi tessellations to compute the structural order in the system defined as follows:

$$S_{\text{vor}} = \langle -zP_z \ln P_z \rangle \quad (6)$$

where  $P_z$  denotes the fraction of Voronoi polygons with coordination number  $z$ , and  $\langle \dots \rangle$  denotes an average over at least 100 evenly spaced simulation snapshots. This entropy measures the deviation of the observed Voronoi cell distribution from that of an ideal single crystal, and therefore vanishes for a perfect hexagonal arrangement. While orientational order parameters and structure factor calculations primarily quantify long-range structural order, Voronoi entropy provides a complementary measure that captures the degree of disorder in the system.

### 2.6 Athermal defect formation simulations

We map the energy landscape of defect formation in a system of  $N = 400$  particles with no thermal fluctuations. To introduce 5-7-7-5 bound dislocation pairs, we select a 6-6-6-6 four-particle cluster composed of two neighboring particles along the  $y$ -axis and their two immediate neighbors along the  $x$ -axis. The system is initialized in a perfect hexagonal configuration. We then actively modulate the interparticle distances  $\tilde{l}_x$  and  $\tilde{l}_y$ , defined as the separations between opposite particles in the  $x$  and  $y$  directions of the chosen four-particle cluster, while allowing all surrounding particles to relax in order to minimize



the total energy. Specifically, we vary  $\tilde{\lambda}_y$  first while keeping  $\tilde{\lambda}_x$  fixed, and then vary  $\tilde{\lambda}_x$  for each chosen value of  $\tilde{\lambda}_y$ . We compute the energy of the relaxed system in the  $\tilde{\lambda}_x - \tilde{\lambda}_y$  plane.

## 2.7 Normal mode analysis

We perform normal mode analysis to characterize the collective vibrational (phonon) modes of a system of  $N = 3600$  particles arranged in a perfect hexagonal configuration. To do so, we construct the Hessian matrix from the second derivatives of the total energy with respect to particle displacements using the following expression:

$$\tilde{H}_{\mu\nu}^{ij} = \frac{\delta^2 \tilde{E}}{\delta \tilde{u}_i^\mu \delta \tilde{u}_j^\nu} \quad (7)$$

where the indices  $ij$  are particle identity,  $\mu/\nu$  are the Cartesian coordinate directions,  $\tilde{u}$  is particle displacement, and  $\tilde{E}$  is the total energy computed using eqn (2). We use a finite difference method to quantify the second derivatives. The Hessian matrix is of the size  $2N \times 2N$  for two-dimensional system. The Hessian eigenvectors  $V_n$  correspond to the normal modes denoted by  $n$ , describing the relative directions and amplitudes of motion for each particle, while we associate the eigenvalues  $\tilde{\lambda}_n$  with the squared frequencies  $\tilde{\omega}_n^2$  of these collective vibrations *i.e.*,  $\tilde{\omega}_n = \sqrt{\tilde{\lambda}_n}$ . Since our physical system with thermal fluctuations is overdamped, this analysis instead provides the eigenvectors and eigenfrequencies of a corresponding “shadow system” that retains the same interparticle interactions but neglects damping.

We also characterize normal modes of an analogous system of a 2D elastic spring network connecting point masses forming the hexagonal crystal lattice. The springs are Hookean and only connect the nearest neighbors. The total energy of the spring network  $\tilde{E}_{\text{spring}}$  is computed using

$$\tilde{E}_{\text{spring}} = \sum_{i'=1}^{2N} \left[ \tilde{k}_{\text{spring}} (\tilde{\ell}_{i'} - \tilde{\ell}_0)^2 \right] \quad (8)$$

where  $i'$  is the spring identity,  $2N$  is the total number of springs connecting  $N$  point masses,  $\tilde{k}_{\text{spring}}$  is spring constant and set to one,  $\tilde{\ell}_{i'}$  is the instantaneous length of the spring  $i'$ , and  $\tilde{\ell}_0$  is the equilibrium spring length corresponding to the nearest-neighbor distance in the ground state of the hexagonal crystal

lattice. We follow the same procedure as outlined above to obtain information about different collective modes.

For each mode  $n$ , the displacement amplitude was drawn from a normal distribution with zero mean and variance  $\langle \tilde{a}_n^2 \rangle = 1/\tilde{\lambda}_n$ , consistent with equipartition. Excluding near-zero eigenvalues associated with translational modes, the total displacement field was constructed as a linear combination  $\tilde{u} = \sum_n \tilde{a}_n V_n$ . Particle positions were then updated by displacing particles by  $\tilde{u}$  from the perfect hexagonal crystal lattice. Repeated sampling produced an ensemble of imperfect hexagonal crystal configurations, which allowed us to compute  $\Psi_6$ .

In a nearly perfect hexagonal crystal, particle displacements give rise to minor distortions of the Voronoi cells from regular hexagons. To quantify these distortions, we computed the probability distribution of the vertex angles  $\theta_{ij}$ . The resulting distribution is hexamodal, with each peak centered around  $(j - 1)\pi/3$ , where  $j \in [1, 6]$  indexes the six-fold symmetry directions. A representative probability distribution is shown in Fig. S3 in the SI. The standard deviations of the six modes are nearly identical, and their average value, denoted as  $\delta$ , is used as a measure of the overall angular distortion in the system configurations. We compute  $\delta$  for the imperfect hexagonal crystal configurations obtained from normal mode analysis and for  $\tilde{k} = 1000$ ,  $\tilde{k} = 100$ , and  $\tilde{k} = 30$  thermal systems in the large- $\gamma$  limit. Building on this angular-deviation framework, we next examine its implications for the bond-orientational order parameter. Using eqn (4), we calculate the local bond-orientational order parameter of a single distorted Voronoi cell by sampling vertex angle,  $\theta_j$ , from a normal distribution with mean  $(j - 1)\pi/3$ , where  $j \in [1, 6]$  and variance  $\delta^2$ . The global bond-orientational order parameter  $\Psi_6$  is then evaluated by averaging local bond-orientational order parameters over at least 1000 individual Voronoi polygon configurations.

## 3 Results and discussion

### 3.1 Order-disorder transition

Our model system shows an order-disorder transition (ODT) when  $\tilde{\gamma}$  is varied at a fixed  $\tilde{k}$ . Fig. 1a and b shows the representative simulation snapshots of the  $\tilde{k} = 1000$  system equilibrated at  $\tilde{\gamma} = 8$  and  $\tilde{\gamma} = 6$ , above and below the ODT  $\tilde{\gamma}$  point,

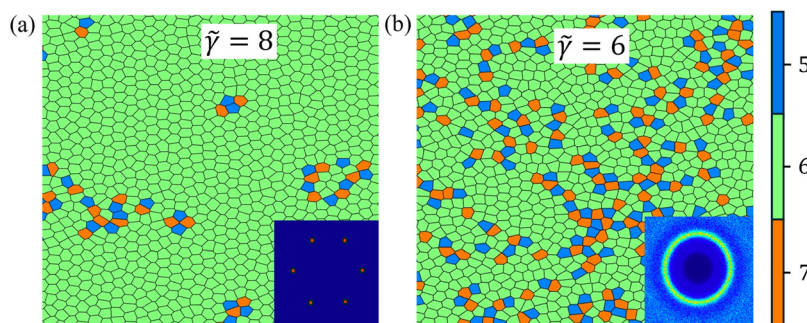


Fig. 1 Representative simulation snapshots of the  $\tilde{k} = 1000$  system at (a)  $\tilde{\gamma} = 8$  and (b)  $\tilde{\gamma} = 6$ . The simulated scattering profile is also shown in the bottom right corner of each figure. Particles are color-coded based on their coordination numbers  $z$ .



respectively. The 2D scattering profile for each state is also shown in the bottom right corner of each snapshot. In the case of  $\tilde{\gamma} = 8$ , the presence of six Bragg peaks exhibiting a six-fold symmetry indicates that the system is in a hexagonally ordered phase, with particle Voronoi centers arranged on a hexagonal crystal lattice. On the other hand, at  $\tilde{\gamma} = 6$ , we see an isotropic ring in the scattering profile which indicates a disordered phase with no crystal symmetry associated with the arrangement of particles.

To obtain an estimate of the location of the ODT in the  $\tilde{\gamma}$  parameter space at a fixed  $\tilde{k}$ , we compute the azimuthally averaged structure factor  $S(\tilde{q})$  from the 2D scattering pattern (see Section 2.3 in Materials and methods). Fig. 2a shows the qualitative comparison of  $S(\tilde{q})$  obtained at three values of  $\tilde{\gamma}$  near the transition. At large  $\tilde{\gamma}$ , for example  $\tilde{\gamma} = 10$ ,  $S(\tilde{q})$  has the clear primary peak at  $\tilde{q}_1 \approx 6.8$ , secondary peak at  $\tilde{q}_2 \approx 11.7 \approx \sqrt{3}\tilde{q}_1$ , and so on, confirming the existence of the underlying hexagonal arrangement of particles. As we decrease  $\tilde{\gamma}$  (increasing relative thermal energy) of the system, the peak heights in  $S(\tilde{q})$  decrease gradually indicating the weakening of the hexagonal order in the system. When  $\tilde{\gamma}$  is small enough (relative thermal energy is high enough), we see a jump in the peak heights with respect to  $\tilde{\gamma}$  at the ODT as the system transitions into the disordered phase from the ordered phase. The persistence of finite peak heights even when the system is globally disordered indicates a short-range liquid-like packing, which is due to the excluded size interaction between particles (*i.e.*,  $\tilde{k}$  is non-zero). This trend can be seen more clearly if we track the primary peak height extracted from  $S(\tilde{q})$  with  $\tilde{\gamma}$  (Fig. 2b). Here we have normalized the  $S(\tilde{q})$  of primary peak heights with that of the primary peak height of a perfect hexagonal crystal lattice. We also characterize the ODT in the system using the mean global orientational order parameter,  $\Psi_6$ . Since  $\text{Im}(\Psi_6)$  is negligible in both the disordered phase and the ordered phase, due to the uniform distribution of  $\psi_6$  and the chosen crystal orientation of the initial configuration, respectively, we focus

our analysis on the behavior of  $\text{Re}(\Psi_6)$  (Fig. 2b). When  $\tilde{\gamma}$  is decreased from a large  $\tilde{\gamma}$ , say,  $\tilde{\gamma} = 100$ ,  $\text{Re}(\Psi_6)$  monotonically decreases and corroborates the observation of weakening of the hexagonal order in the system from above analysis. As the system disorders from the ordered state,  $\text{Re}(\Psi_6)$  jumps from 0.25 to approximately zero in the disordered phase, indicating a complete loss of hexagonal symmetry. We estimate the location of the ODT by taking the average of the largest  $\tilde{\gamma}$  at which the system is disordered and the smallest  $\tilde{\gamma}$  at which the system is ordered obtaining  $\tilde{\gamma}_{\text{ODT}} = 6.5$  for the  $\tilde{k} = 1000$  system. We further characterized the order-disorder transition using the bond-orientational correlation function (see the SI for details). The disordered phase exhibits finite bond-orientational correlation lengths, whereas the ordered phase displays long-range correlations (refer to Fig. S4 in the SI). In conclusion, our simple model shows an ODT behavior. We note that studies on such 2D systems have shown the existence of a hexatic phase – sandwiched between disordered and hexagonally ordered phases – with a narrow stability region.<sup>28,46,47</sup> However, we do not observe a hexatic phase in the present study likely due to the moderate system size considered. In two-dimensional systems, intermediate hexatic phases are known to be particularly sensitive to the system size effect,<sup>30,48</sup> and we therefore cannot rule out the possibility that a hexatic phase may emerge in larger systems. With this caveat in mind,  $\tilde{\gamma}_{\text{ODT}}$  is an estimate of location of ODT to a first approximation.

In our model,  $\tilde{k}$  sets the degree of dynamic size-dispersity in the system at a given  $\tilde{\gamma}$  with smaller  $\tilde{k}$  leading to greater size-dispersity among particles. To investigate the impact of dynamic size-dispersity on the ODT, we take  $\tilde{k} = 30$  (high size-dispersity) and  $\tilde{k} = 100$  (moderate size-dispersity) along with  $\tilde{k} = 1000$  (low size-dispersity) systems. The behavior of  $\text{Re}(\Psi_6)$  with  $\tilde{\gamma}$  for these systems is shown in Fig. 3a. We estimate size-dispersity in our system by the standard deviation in particle area from its mean preferred value (which is one in dimensionless units in our simulations), denoted here as  $\tilde{\sigma}_A$ . Fig. 3b shows

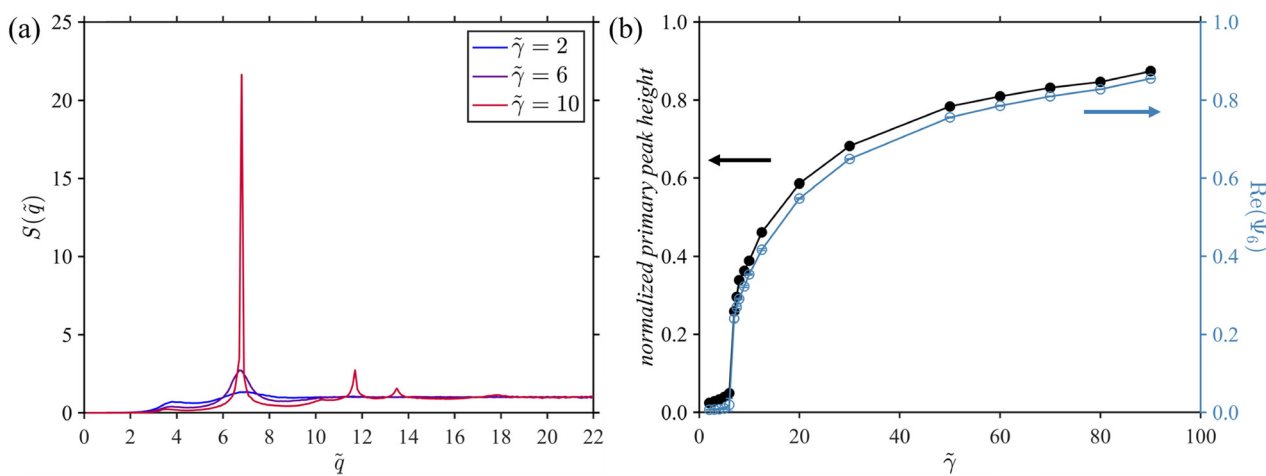


Fig. 2 (a) Azimuthally averaged structure factor  $S(\tilde{q})$  as a function of  $\tilde{q}$  for the  $\tilde{k} = 1000$  system at three values of  $\tilde{\gamma}$ . (b) Normalized primary peak heights of  $S(\tilde{q})$  relative to that of a perfect hexagonal lattice (solid line with closed markers) and mean global orientational order parameter (solid line with open markers) with  $\tilde{\gamma}$ . Both quantities jump at the ODT, which is estimated to be at  $\tilde{\gamma}_{\text{ODT}} = 6.5$ .



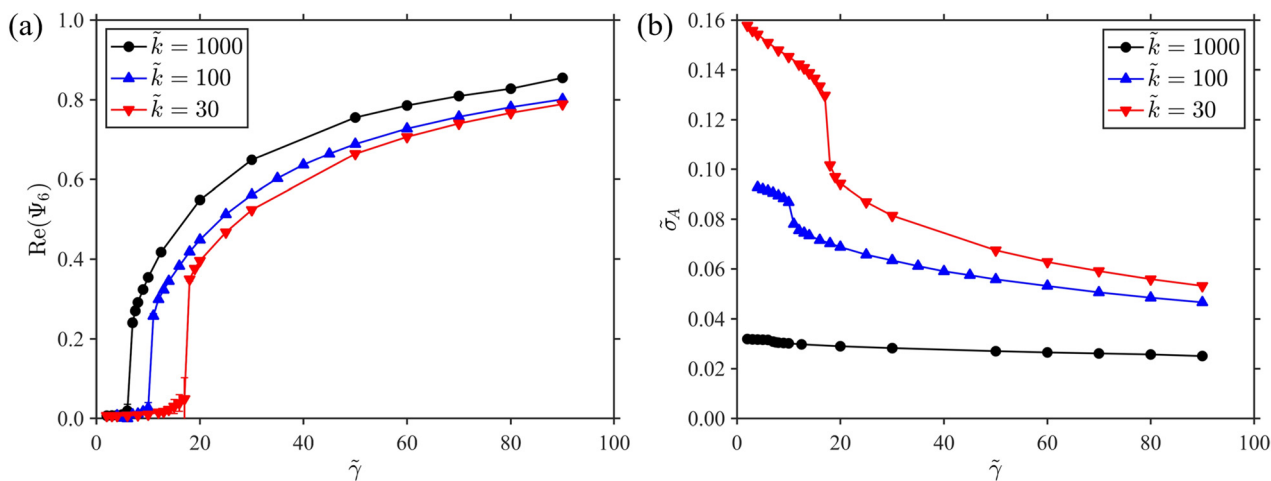


Fig. 3 (a) Mean global orientational order parameter and (b) dynamic size-dispersity between particles for  $\tilde{k} = 1000$ ,  $\tilde{k} = 100$ , and  $\tilde{k} = 30$  systems with  $\tilde{\gamma}$ .

the variation of  $\sigma_A$  with  $\tilde{\gamma}$  for three systems. Similar to the  $\tilde{k} = 1000$  system, the other two systems with  $\tilde{k} = 100$  and  $\tilde{k} = 30$  also show the ODT when  $\tilde{\gamma}$  is modulated (Fig. 3a). Apart from that, we also observe a monotonic decrease in  $\tilde{\gamma}_{\text{ODT}}$  with  $\tilde{k}$ . The estimate of  $\tilde{\gamma}_{\text{ODT}}$  is 17.5 for  $\tilde{k} = 30$  and 10.5 for  $\tilde{k} = 100$  systems along with 6.5 for the  $\tilde{k} = 1000$  system. The bond-orientational correlation function analysis for the three systems is also shown in Fig. S4. Qualitatively, the trend can be explained by considering two effects. First, increasing dynamic size-dispersity in our model enhances the configurational entropy of the disordered phase, as the disordered system can access an enormous number of distinct Voronoi tessellations. This entropic gain stabilizes the disordered phase relative to the ordered phase shifting the ODT. A similar stabilization mechanism has been observed in experiments<sup>49</sup> and simulations<sup>50</sup> of three-dimensional colloidal systems with static polydispersity, as well as in computational studies of hard disks with static polydispersity,<sup>32</sup> where permutations of particle sizes introduce

additional degrees of freedom that increase the configurational entropy of the fluid phase.<sup>51,52</sup> Second, for our system at a given  $\tilde{k}$ , increasing  $\tilde{\gamma}$  reduces size-dispersity (Fig. 2b). This result is a direct consequence of our energy expression (eqn (2)) where the ground state is the perfect hexagonal crystal lattice. At a given  $\tilde{k}$ , increasing  $\tilde{\gamma}$  moves the system closer to the ground state, while simultaneously driving the particle size and shape closer to a regular hexagon of unit area (in dimensionless units). Thus, in our model, the ordered phase is energetically favored while the disordered phase is entropically favored. Taken together, a higher  $\tilde{\gamma}_{\text{ODT}}$  is observed for systems with lower  $\tilde{k}$ .

At a given  $\tilde{k}$ ,  $\tilde{\gamma}$  not only affects the size-dispersity but also the shape of the particles. To gain a deeper understanding of the microscopic mechanisms underlying the transition, we computed  $\langle |\psi_6| \rangle$  which is a measure of the mean degree of hexagonality of particles in the assembly and show its dependence on  $\tilde{\gamma}$  in Fig. 4a. We also computed  $\langle |\psi_6| \rangle$  for random Voronoi tessellation where Voronoi centers were generated

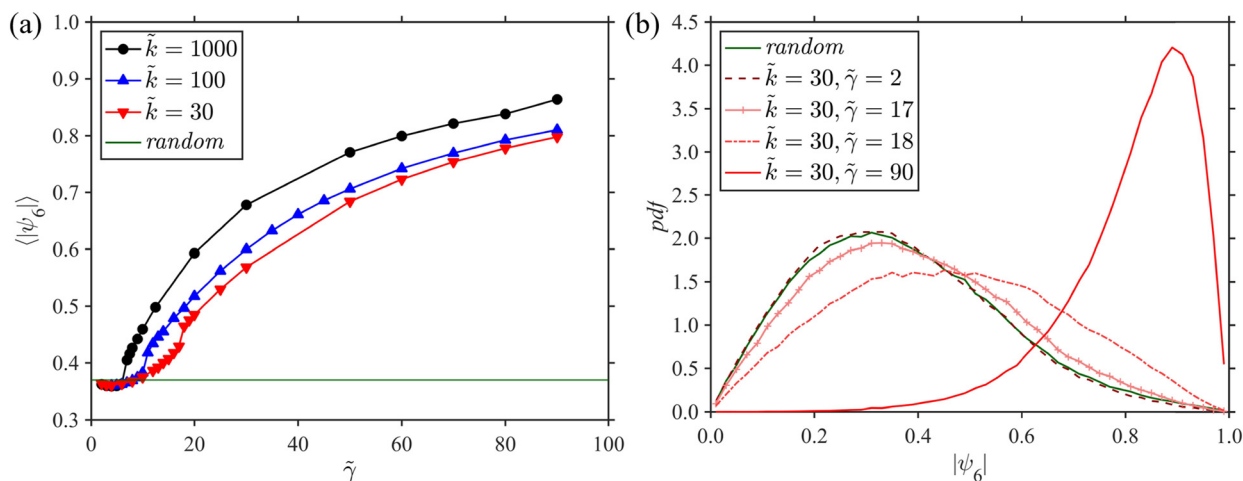


Fig. 4 (a) Mean degree of hexagonality of particles  $\langle |\psi_6| \rangle$  with  $\tilde{\gamma}$  for  $\tilde{k} = 1000$ ,  $\tilde{k} = 100$ ,  $\tilde{k} = 30$ , and random Voronoi tessellation. Error bars are smaller than the marker size. (b) Probability density function (pdf) of  $|\psi_6|$  for the  $\tilde{k} = 30$  system at  $\tilde{\gamma} = 2$ , at  $\tilde{\gamma} = 17$  in the disordered phase, and at  $\tilde{\gamma} = 18$  and  $\tilde{\gamma} = 90$  in the ordered phase along with the distribution of  $|\psi_6|$  for random Voronoi tessellation.



randomly (Poisson distribution) in the simulation box. In line with Fig. 3,  $\langle |\psi_6| \rangle$  shows a jump with respect to  $\tilde{\gamma}$  at the ODT; however, the jump is less sharp. Below the ODT in the disordered phase, these three systems merge onto the common branch of  $\langle |\psi_6| \rangle$  with  $\tilde{\gamma}$ . As  $\tilde{\gamma}$  is decreased further and approaches zero,  $\langle |\psi_6| \rangle$  for all the system saturates to about 0.36 which is close to 0.37 computed for random Voronoi tessellation implying that the arrangement of particles is close to random. The difference is due to the fact that  $\tilde{k}$  is non-zero for three systems leading to excluded-area interactions among particles. The arrangement of particles being approximately random at low  $\tilde{\gamma}$  is also verified by comparing their  $|\psi_6|$  distribution against that of random Voronoi tessellation shown in Fig. 4b. The signature of ODT is also evident from the pronounced changes in the  $|\psi_6|$  distribution across the transition, reflecting the collective rearrangement of particle shapes as the system approaches ODT. Due to the deformable nature of particles and thermal fluctuations, even deep into the ordered phase, a non-negligible population of particles adopt irregular hexagonal shapes as indicated by the shape distribution for the  $\tilde{k} = 30$  system at  $\tilde{\gamma} = 90$ .

Particle shape and size distributions both influence the ODT in deformable particle systems. Notably, the  $\langle |\psi_6| \rangle$  for the  $\tilde{k} = 30$  system at  $\tilde{\gamma} = 17$  in the disordered phase exceeds that of the  $\tilde{k} = 1000$  system at  $\tilde{\gamma} = 7$  in the ordered phase, shown in Fig. 4a. This suggests that large size dispersity can suppress long-range order even when many particles exhibit a high  $|\psi_6|$ . An open question is: what is the upper limit of  $\langle |\psi_6| \rangle$  that still permits disorder due to size dispersity? The coupled effects of particle size and shape on phase behavior will be examined in future work.

We also characterize the structural order in the system by measuring the Voronoi entropy of the particle assembly. This analysis has proven useful in analyzing 2D point patterns.<sup>53,54</sup> We emphasize that  $S_{\text{vor}}$  is an intensive quantity, whereas thermodynamic entropy is extensive. In Fig. 5, we report  $S_{\text{vor}}$  as a function of  $\tilde{\gamma}$  for three systems, along with results for a

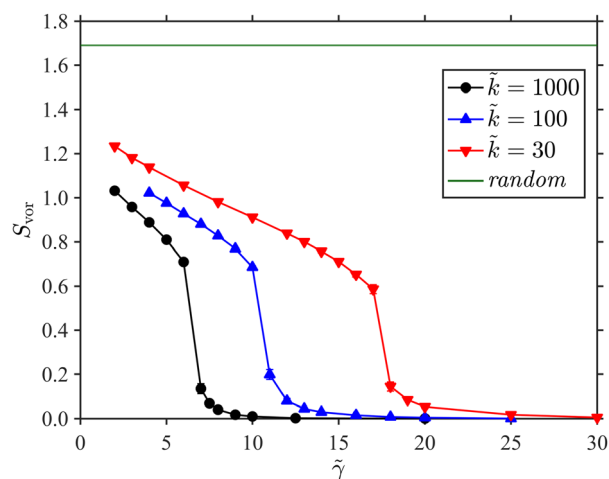


Fig. 5 Voronoi entropy  $S_{\text{vor}}$  with  $\tilde{\gamma}$  for  $\tilde{k} = 1000$ ,  $\tilde{k} = 100$ , and  $\tilde{k} = 30$  systems, and random Voronoi tessellation.

random Voronoi tessellation. For the random Voronoi tessellation, we compute  $S_{\text{vor}} \approx 1.69$ , consistent with values reported in the literature.<sup>54,55</sup> Consistent with the trends discussed above,  $S_{\text{vor}}$  exhibits discontinuous changes at the ODT: the disordered phase is characterized by a higher entropy, while the hexagonal ordered phase exhibits a lower entropy. At the same  $\tilde{\gamma}$ , systems with a greater dynamic size dispersity (or lower  $\tilde{k}$ ) display a higher entropy, indicating that size dispersity promotes structural disorder. Random Voronoi tessellation serves as the limiting behavior of our system indicating that lowering  $\tilde{k}$  and  $\tilde{\gamma}$  drive the system closer to the random Voronoi tessellation.

### 3.2 Defect formation

The structural disorder in the ordered phase in our system arises from the presence of topological defects. A defect is defined as a particle whose number of sides (or neighbors) is different from 6. Since particles in 2D assembly are less correlated compared to their 3D analog, defects spontaneously form and annihilate in the assembly, and there exists a non-zero equilibrium concentration of defects in the system.<sup>27,56</sup> These defects are generated by structural rearrangement of particles in succession such that two adjacent particles swap their neighbors, called T1 topological events/transitions. A T1 event transforms a four-particle cluster of six-sided particles (6–6–6–6) into a cluster of 5–7–7–5-sided particles, forming what are known as bound dislocation pairs. The introduction of such dislocation pairs into a crystal creates singularities in the underlying local order parameter field, thereby disrupting the local structural order. We estimate the concentration of topological defects in the ordered phase,  $f_{\text{def}}$ , by calculating the fraction of non-hexagonal particles, which is the ratio of non-hexagonal particles to the total number of particles. Topological defects are not defined in the static disordered configurations due to the absence of an underlying crystal lattice; however, the fraction of non-hexagonal particles can still be quantified. Fig. 6 shows the variation of  $f_{\text{def}}$  with  $\tilde{\gamma}$ . Far from the ODT in the ordered phase, we see a negligible concentration of defects in all the systems; however, the defect concentration exponentially increases (inset of Fig. 6) as the system approaches the ODT followed by melting of the crystalline order.

This observation is reminiscent of the defect-mediated melting in 2D described by the Kosterlitz–Thouless–Halperin–Nelson–Young theory.<sup>27,57,58</sup> The exponential dependence of defect concentration on  $\tilde{\gamma}$  indicates that defect formation and annihilation follow Arrhenius-type behavior, with the slope of the best-fit line providing an estimate of the activation barrier. Similar behavior has been reported in neighbor exchange events in a disordered cell monolayer studied using the Vertex model.<sup>59</sup> From the inset, the slopes follow the order  $\tilde{k} = 1000 > \tilde{k} = 100 > \tilde{k} = 30$ , implying that defect formation becomes easier as  $\tilde{k}$  decreases.

To gain insights into defect formation in our thermal system, we take a simpler system of a perfect hexagonal crystal with no thermal fluctuation. We then perform a T1 transition to create 5–7–7–5 dislocation pairs. To do so, we modulate  $\tilde{l}_x$  and



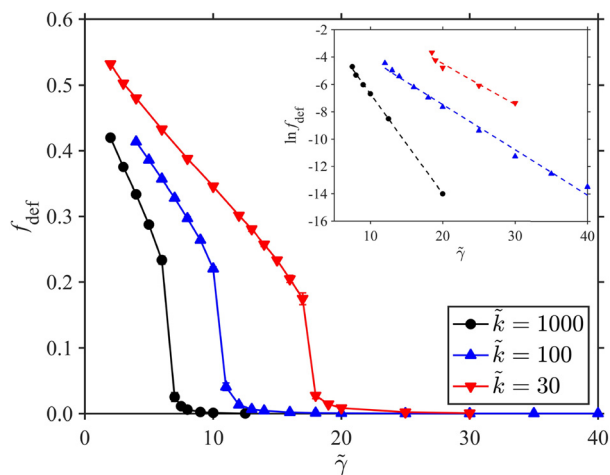


Fig. 6 Concentration of topological defects  $f_{\text{def}}$  with  $\tilde{\gamma}$  for  $\tilde{k} = 1000$ ,  $\tilde{k} = 100$ , and  $\tilde{k} = 30$  systems. The inset shows the linear fit on  $\ln f_{\text{def}}$  with  $\tilde{\gamma}$  for three systems. The solid markers are the data points, and dashed lines are the best fit.

$\tilde{l}_y$ , interparticle distances of opposite particles in the  $x$  and  $y$  directions in the four-particle configuration shown in the top panel of Fig. 7c, respectively, and minimize the energy of the surrounding particles (see Section 2.6 in Materials and methods). This procedure allows us to create defects in a controlled manner while looking at the underlying energy landscape of defect formation. We compute contour maps of the system energies relative to the ground state, *i.e.*, the total energy minus the energy of the ground state of the hexagonal crystal lattice, in the  $\tilde{l}_x - \tilde{l}_y$  plane for the three cases of  $\tilde{k}$  at  $\tilde{\gamma} = 20$ . These systems are ordered under these conditions when thermalized (see Fig. 3). Both  $\tilde{k} = 30$  and  $\tilde{k} = 100$  systems show a metastable defect-state with respect to the perfect hexagonal state (global energy minimum); however, we do not see any signature of

metastable defect-state for the  $\tilde{k} = 1000$  case (refer to Fig. S5 in the SI for energy contour maps for  $\tilde{k} = 100$  and  $\tilde{k} = 1000$ ). We extract the energy barrier heights at the T1 transition as a function of  $\tilde{l}_x$  along the  $\tilde{l}_x = \tilde{l}_y$  line for the three cases of  $\tilde{k}$ . Note that  $\tilde{l}_x$  is equal to  $\tilde{l}_y$  at the T1 transition. We show the comparison of energy barriers in Fig. 6b. The minima of the energy barrier curves denote the intersection of the minimum-energy paths (MEPs) taken by the system to form defects starting from the perfect hexagonal state. We observe that the energy barrier height along the MEP increases with  $\tilde{k}$  suggesting that it becomes increasingly improbable to form defects when  $\tilde{k}$  is increased. Moreover, the curvature of the energy barrier around its minima is also affected by the value of  $\tilde{k}$ . A large value of  $\tilde{k}$  sets a higher curvature of energy barrier around the MEP indicating that other energy pathways taken by the system on the energy landscape to form defects through T1 transition become less probable with increase in  $\tilde{k}$ . This analysis likely suggests that a larger  $\tilde{k}$  suppresses the defect formation in our thermal systems at a given  $\tilde{\gamma}$ , giving a potential explanation why the ODT for larger  $\tilde{k}$  values occurs at smaller  $\tilde{\gamma}$  values.

### 3.3 Far from the ODT

In a crystalline solid at finite temperature, atoms are not stationary but undergo collective vibrations, known as phonons, with frequencies determined by the interatomic potential and thermal energy. We expect analogous phonon-like behavior in our system, particularly far from the ODT in the ordered phase. Because our system is overdamped, this should manifest as similar displacement fields in the particle configurations. To probe these modes, we perform normal mode analysis on our system (see Section 2.7 in Materials and methods). For a two-dimensional crystal, the Debye model predicts that the cumulative number of normal modes scales with the square of the

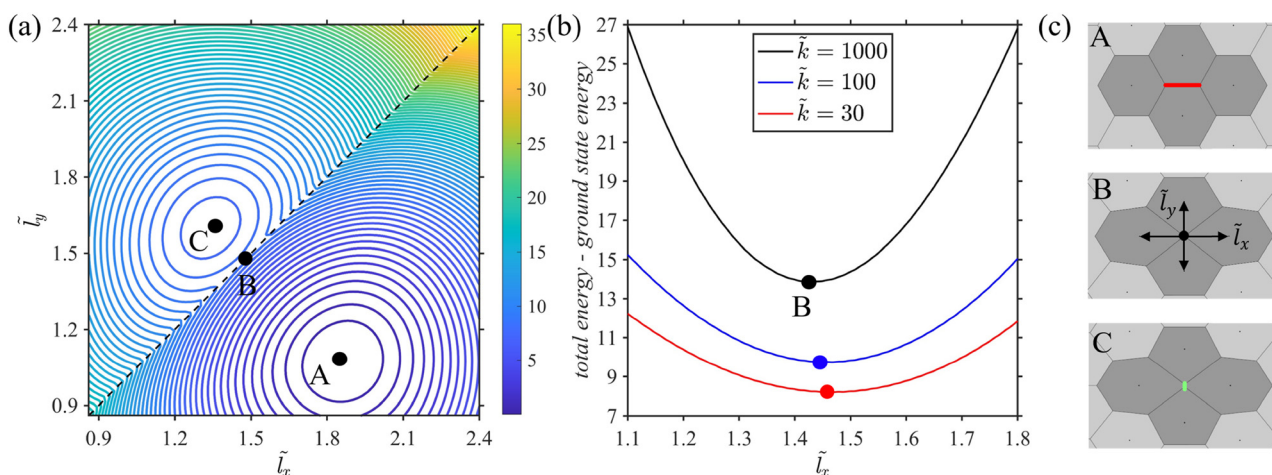


Fig. 7 (a) Contour maps of the system energies relative to the ground state, *i.e.*, the total energy minus the energy of the ground state of the hexagonal crystal lattice, in the  $\tilde{l}_x - \tilde{l}_y$  plane at  $\tilde{\gamma} = 20$  and  $\tilde{k} = 30$ . The dashed line is drawn at  $\tilde{l}_x = \tilde{l}_y$ , which is at the T1 transition. (b) Total energy minus the energy of the hexagonal state at the T1 transition as a function of  $\tilde{l}_x$  where  $\tilde{l}_x = \tilde{l}_y$  at  $\tilde{\gamma} = 20$  for  $\tilde{k} = 30$ ,  $\tilde{k} = 100$ , and  $\tilde{k} = 1000$ . The closed circles indicate the minimum of the curve. (c) Top panel A represents the perfect hexagonal state, middle panel B is the representative configuration at the T1 transition, and bottom panel C is a representative configuration of a defect-state.



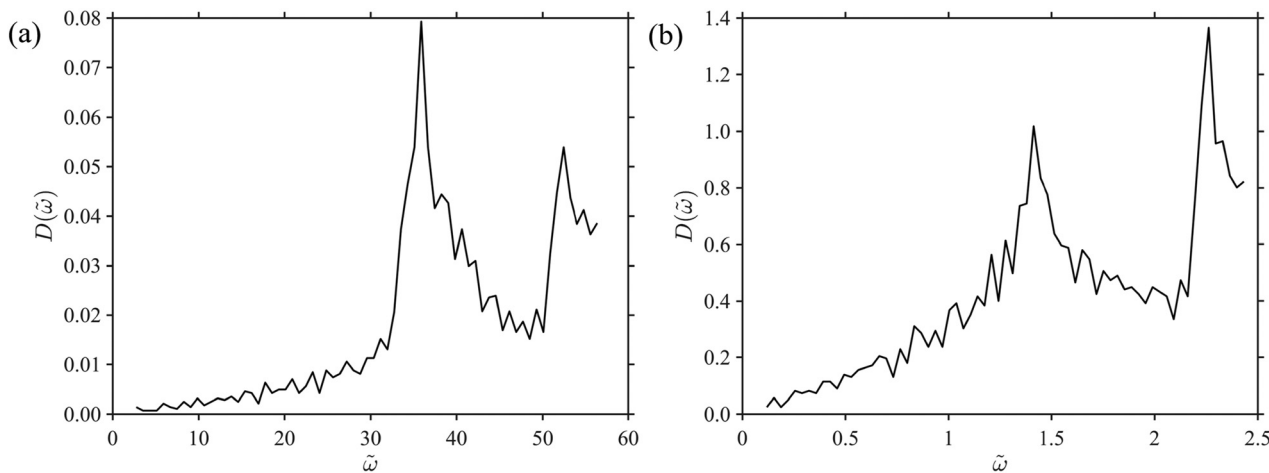


Fig. 8 Phonon density of states,  $D(\tilde{\omega})$ , with normal mode frequency,  $\tilde{\omega}$  for (a) the Voronoi model with  $\tilde{k} = 100$  and  $\tilde{\gamma} = 500$  and (b) a harmonic spring network with pair-wise interactions with a spring constant of 1 (in dimensionless units).

frequency in the low-frequency regime.<sup>60</sup> Our model conforms with the Debye model in large- $\tilde{\gamma}$  limit as shown in Fig. S6 in the SI. In this limit, we also expect that the many-body interactions will be negligible since particles vibrate around the lattice positions with small displacements, and the coupled interparticle interactions in our model will effectively converge to harmonic interactions. In other words, the Voronoi model should behave as a harmonic spring network model in the large- $\tilde{\gamma}$  regime. To test this hypothesis, we compare the phonon density of states,  $D(\tilde{\omega})$ , of our crystal system with that of a harmonic spring network, as shown in Fig. 8. We observe two divergent peaks in  $D(\tilde{\omega})$  for the Voronoi model, consistent with the prediction of two van Hove singularities in  $D(\tilde{\omega})$  for a two-dimensional hexagonal crystal, corresponding to the longitudinal and transverse modes.<sup>61</sup> A similar feature is observed in  $D(\tilde{\omega})$  for the harmonic spring network model.

Furthermore, we estimated the displacements of all particles in the Voronoi system from their corresponding lattice positions using the Hessian eigenvalues and eigenvectors (see Section 2.7 in Materials and methods). Applying these displacement fields to the perfect hexagonal lattice generated ensembles of perturbed configurations, from which  $\Psi_6$  was computed. In the absence of defects, thermal energy in an undamped system drives collective oscillations of particles, and similarly, we expect collective particle displacements in our thermal systems far from the ODT, *i.e.*,  $\tilde{\gamma} > 50$ —where the defect concentration is negligible—to be governed purely by thermal energy. To test this, we compared  $\text{Re}(\Psi_6)$  obtained from normal mode analysis with the results from thermal simulations at  $\tilde{k} = 1000$ ,  $\tilde{k} = 100$ , and  $\tilde{k} = 30$  (Fig. 9), where the  $x$ -axis represents the overall angular distortion in the system configurations, denoted as  $\delta$ , defined as the average of the six standard deviations corresponding to the six modes in the hexamodal vertex angle probability distribution (see Section 2.7 in Materials and methods). The close agreement between the thermal systems and normal mode analysis indicates that all  $\tilde{k}$ -systems in the large- $\tilde{\gamma}$  limit exhibit collective particle displacements consistent with the predictions of normal mode theory. We further examined

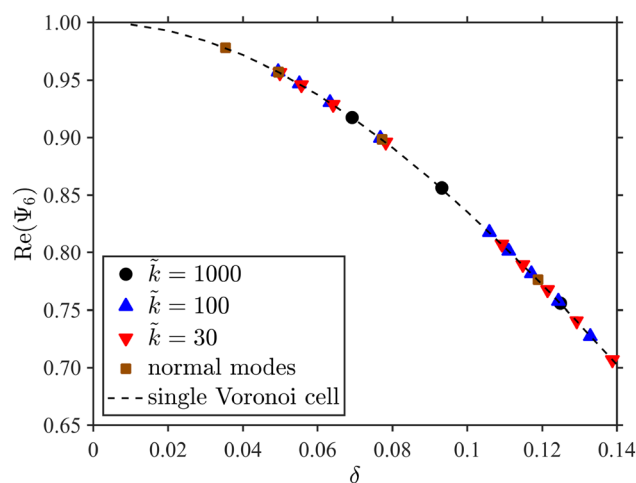


Fig. 9 Mean global orientational order parameter with  $\delta$ , defined as the average of the six standard deviations corresponding to the six modes in the hexamodal vertex angle probability distribution, for the system configurations of  $\tilde{k} = 1000$ ,  $\tilde{k} = 100$ , and  $\tilde{k} = 30$ , for configurations generated by applying displacement fields to a perfect hexagonal lattice from normal mode analysis. Note that  $\tilde{\gamma}$  is variable along the curve for thermal systems with different  $\tilde{k}$  values. Error bars are smaller than the marker size. The dashed line represents the results obtained for a single distorted Voronoi cell, where the vertex angles,  $\theta_j$ , were sampled from a normal distribution with mean  $(j - 1)\pi/3$ , for  $j \in [1, 6]$  and variance  $\delta^2$ .

a case of a single Voronoi cell in which vertex angles are sampled from normal distributions with mean  $(j - 1)\pi/3$  where  $j \in [1, 6]$  and variance  $\delta^2$ , which also reproduced the observed behavior, supporting the conclusion that vertex angular deviations in thermal systems are well described by a normal distribution in the large- $\tilde{\gamma}$  limit.

## 4 Conclusions

In this study, we use a Voronoi model to investigate the packing behavior of soft, deformable particles in two dimensions.



Two model parameters,  $\tilde{\gamma}$  and  $\tilde{k}$ , control particle line tension and dynamic size-dispersity, respectively. Monte Carlo simulations at constant temperature reveal an order–disorder transition: the system forms a hexagonal crystal lattice at high  $\tilde{\gamma}$  and melts into a disordered phase at low  $\tilde{\gamma}$ . The ODT shifts with  $\tilde{k}$ , with lower  $\tilde{k}$  pushing the transition to higher  $\tilde{\gamma}$ . Consistent with previous studies, large size-dispersity (low  $\tilde{k}$ ) suppresses long-range order. Analysis of defect formation in athermal systems through T1 transitions shows that defects form more easily at low  $\tilde{k}$ , with the activation barrier increasing with  $\tilde{k}$ . This is supported by Voronoi entropy and defect concentration measurements, which are higher for low- $\tilde{k}$  systems, reflecting a greater defect content and providing a mechanistic explanation for the observed ODT trends.

We also studied the phonon modes of our system far from the ODT and found that it behaves like a harmonic spring network with pairwise interactions. The vibrational density of states exhibits two van Hove peaks, in agreement with theoretical predictions. The similarity between the vibrational density of states of the Voronoi model and the harmonic spring network suggests that the coupled interactions in the model effectively become pairwise far from the ODT. Furthermore, deviations in the orientational order parameter from that of the hexagonal crystal lattice in this regime, where the defect concentration is negligible, can be well captured by constructing displacement fields from normal mode analysis.

We believe that our model provides a useful conceptual framework for investigating soft-matter systems in which effective particle interactions can be approximated using the energy functional employed in this study. Representative experimental realizations could include emulsions, microgels, or micellar assemblies, where particle deformability plays a central role. In practice, the material parameters such as line tension and resistance to mass exchange between particles along with average particle size would need to be tuned to map onto the dimensionless parameters quantified here. The energy functional considered is also simplified, and realizing an exact quantitative experimental analog could be a limitation of the present simulations. Further deviations between model predictions and experimental observations may arise from non-space-filling particle configurations and from departures from the idealized two-dimensional geometry assumed in our simulations.

## Conflicts of interest

There are no conflicts to declare.

## Data availability

Supplementary information (SI) is available that includes system size analysis, the influence of initial conditions, and bond-orientational correlations across the order–disorder transition, along with other supporting results. See DOI: <https://doi.org/10.1039/d5sm01097g>.

Relevant raw data are available on Zenodo. See DOI: <https://doi.org/10.5281/zenodo.18133950>.

## Acknowledgements

We gratefully thank the support from the National Science Foundation (Grant No. NSF 2230946).

## References

- 1 Y. Zhou, S. L. Bore, A. R. Tao, F. Paesani and G. Arya, *npj Comput. Mater.*, 2023, **9**, 224.
- 2 D. Chintha, S. K. Veeram, E. Boattini, L. Filion and S. N. Punnathanam, *J. Chem. Phys.*, 2021, **155**, 244901.
- 3 G. Carrot, A. E. Harrak, J. Oberdisse, J. Jestin and F. Boué, *Soft Matter*, 2006, **2**, 1043–1047.
- 4 A. Nabiyan, A. Muttathukattil, F. Tomazic, D. Pretzel, U. S. Schubert, M. Engel and F. H. Schacher, *ACS Nano*, 2023, **17**, 21216–21226.
- 5 F. Zeng and S. C. Zimmerman, *Chem. Rev.*, 1997, **97**, 1681–1712.
- 6 Z. Lyu, L. Ding, A. Tintaru and L. Peng, *Acc. Chem. Res.*, 2020, **53**, 2936–2949.
- 7 O. Altintas, G. Hizal and U. Tunca, *J. Polym. Sci., Part A: Polym. Chem.*, 2006, **44**, 5699–5707.
- 8 K. Hayashida, T. Dotera, A. Takano and Y. Matsushita, *Phys. Rev. Lett.*, 2007, **98**, 195502.
- 9 J. Buitenhuis and S. Förster, *J. Chem. Phys.*, 1997, **107**, 262–272.
- 10 R. A. Segalman, A. Hexemer, R. C. Hayward and E. J. Kramer, *Macromolecules*, 2003, **36**, 3272–3288.
- 11 I. W. Hamley, C. Daniel, W. Mingvanish, S.-M. Mai, C. Booth, L. Messe and A. J. Ryan, *Langmuir*, 2000, **16**, 2508–2514.
- 12 V. Vitkova, M. Mader and T. Podgorski, *Europhys. Lett.*, 2004, **68**, 398.
- 13 E. L. Romero and M. J. Morilla, *Int. J. Nanomed.*, 2013, **8**, 3171–3186.
- 14 Y. Peng, Z. Wang, A. M. Alsayed, A. G. Yodh and Y. Han, *Phys. Rev. Lett.*, 2010, **104**, 205703.
- 15 M. R. Islam, R. Nguyen and L. A. Lyon, *Macromol. Rapid Commun.*, 2021, **42**, 2100372.
- 16 H.-Y. Chang, Y.-J. Sheng and H.-K. Tsao, *J. Mol. Liq.*, 2022, **364**, 120025.
- 17 Y.-H. Tsao, S.-K. Li, H.-K. Tsao and Y.-J. Sheng, *Colloids Surf., A*, 2024, **680**, 132656.
- 18 I. M. Van Meerbeek, B. C. Mac Murray, J. W. Kim, S. S. Robinson, P. X. Zou, M. N. Silberstein and R. F. Shepherd, *Adv. Mater.*, 2016, **28**, 2801–2806.
- 19 D. L. Barton, S. Henkes, C. J. Weijer and R. Sknepnek, *PLoS Comput. Biol.*, 2017, **13**, e1005569.
- 20 D. Bi, J. H. Lopez, J. M. Schwarz and M. L. Manning, *Soft Matter*, 2014, **10**, 1885–1890.



- 21 A. Scotti, M. Brugnoli, A. A. Rudov, J. E. Houston, I. I. Potemkin and W. Richtering, *J. Chem. Phys.*, 2018, **148**, 174903.
- 22 Y. Jin and H. A. Makse, *Phys. A*, 2010, **389**, 5362–5379.
- 23 A. Donev, S. Torquato, F. H. Stillinger and R. Connelly, *J. Appl. Phys.*, 2004, **95**, 989–999.
- 24 S.-C. Mau and D. A. Huse, *Phys. Rev. E:Stat., Nonlinear, Soft Matter Phys.*, 1999, **59**, 4396–4401.
- 25 L. Sun, Z. Li, Y. Zhang, Y. Lu and S. Zhang, *Prog. Mater. Sci.*, 2026, **155**, 101531.
- 26 S. Hou, L. Bai, D. Lu and H. Duan, *Acc. Chem. Res.*, 2023, **56**, 740–751.
- 27 B. I. Halperin and D. R. Nelson, *Phys. Rev. Lett.*, 1978, **41**, 121–124.
- 28 S. C. Kapfer and W. Krauth, *Phys. Rev. Lett.*, 2015, **114**, 035702.
- 29 R. Guo, J. Li and B. Ai, *Phys. A*, 2023, **623**, 128833.
- 30 E. P. Bernard and W. Krauth, *Phys. Rev. Lett.*, 2011, **107**, 155704.
- 31 P. Sampedro Ruiz and R. Ni, *J. Chem. Phys.*, 2020, **153**, 174501.
- 32 P. Sampedro Ruiz, Q. Lei and R. Ni, *Commun. Phys.*, 2019, **2**, 70.
- 33 S.-H. Choi, F. S. Bates and T. P. Lodge, *Macromolecules*, 2011, **44**, 3594–3604.
- 34 I. Bouhid de Aguiar, T. van de Laar, M. Meireles, A. Bouchoux, J. Sprakel and K. Schroën, *Sci. Rep.*, 2017, **7**, 10223.
- 35 E. Boattini, N. Bezem, S. N. Punnathanam, F. Smallenburg and L. Fillion, *J. Chem. Phys.*, 2020, **153**, 064902.
- 36 A. Boromand, A. Signoriello, F. Ye, C. S. O'Hern and M. D. Shattuck, *Phys. Rev. Lett.*, 2018, **121**(24), 248003.
- 37 M. A. Spencer, Z. Jabeen and D. K. Lubensky, *Eur. Phys. J. E:Soft Matter Biol. Phys.*, 2017, **40**, 2.
- 38 D. M. Sussman, *Comput. Phys. Commun.*, 2017, **219**, 400–406.
- 39 I. Tah, D. Haertter, J. M. Crawford, D. P. Kiehart, C. F. Schmidt and A. J. Liu, *Proc. Natl. Acad. Sci. U. S. A.*, 2025, **122**, e2322732121.
- 40 Y.-W. Li, L. L. Y. Wei, M. Paoluzzi and M. P. Ciamarra, *Phys. Rev. E*, 2021, **103**, 022607.
- 41 D. Bi, X. Yang, M. C. Marchetti and M. L. Manning, *Phys. Rev. X*, 2016, **6**, 021011.
- 42 K. Brakke, R. Phelan and D. Weaire, *Exp. Math.*, 1995, **4**, 181–192.
- 43 T. O. Bello, S. Lee and P. T. Underhill, *Soft Matter*, 2022, **18**, 5106–5113.
- 44 delaunayTriangulation – Delaunay triangulation in 2-D and 3-D – MATLAB, <https://www.mathworks.com/help/matlab/ref/delaunaytriangulation.html>, (accessed 29 September 2025).
- 45 T. C. Hales, *Discrete Comput. Geom.*, 2001, **25**, 1–22.
- 46 M. Durand and J. Heu, *Phys. Rev. Lett.*, 2019, **123**, 188001.
- 47 S. Prestipino, F. Saija and P. V. Giaquinta, *Phys. Rev. Lett.*, 2011, **106**, 235701.
- 48 N. Gribova, A. Arnold, T. Schilling and C. Holm, *J. Chem. Phys.*, 2011, **135**, 054514.
- 49 H. J. Schöpe, G. Bryant and W. van Meegen, *Phys. Rev. E*, 2006, **74**(6), 060401.
- 50 M. Cerbelaud, F. Mortier, H. Semaan, J. Gerhards, B. Crespini, R. Ferrando and A. Videcoq, *Mater. Today Commun.*, 2024, **38**, 107973.
- 51 M. Ozawa, G. Parisi and L. Berthier, *J. Chem. Phys.*, 2018, **149**, 154501.
- 52 M. Ozawa and L. Berthier, *J. Chem. Phys.*, 2017, **146**, 014502.
- 53 E. Bormashenko, M. Frenkel, A. Vilks, I. Legchenkova, A. A. Fedorets, N. E. Aktaev, L. A. Dombrovsky and M. Nosonovsky, *Entropy*, 2018, **20**, 956.
- 54 D. Paulovics, E. Bormashenko, C. Raufaste and F. Celestini, *Phys. Rev. E*, 2024, **110**, 024302.
- 55 E. Bormashenko, I. Legchenkova and M. Frenkel, *Entropy*, 2019, **21**, 452.
- 56 A. Pertsinidis and X. S. Ling, *Phys. Rev. Lett.*, 2001, **87**, 098303.
- 57 J. M. Kosterlitz and D. J. Thouless, *J. Phys. C-Solid State Phys.*, 1973, **6**, 1181.
- 58 A. P. Young, *Phys. Rev. B:Condens. Matter Mater. Phys.*, 1979, **19**, 1855–1866.
- 59 D. Bi, J. H. Lopez, J. M. Schwarz and M. L. Manning, *Soft Matter*, 2014, **10**, 1885–1890.
- 60 A. Ghosh, R. Mari, V. K. Chikkadi, P. Schall, A. C. Maggs and D. Bonn, *Phys. A*, 2011, **390**, 3061–3068.
- 61 L. Van Hove, *Phys. Rev.*, 1953, **89**, 1189–1193.

